D-6142
[1-10]

RESEARCH ARTICLE Agricultural Science Digest, Volume Issue : ()

# Synthesis and Characterization of Ca, Mg, Fe and Zn Nanoparticles and its Impact on *Bacillus thuringiensis*

M. Gayathri[1,2], N.C. Venkateswarlu[1], T. N.V.K.V. Prasad[3]

10.18805/ag.D-6142

## ABSTRACT

**Background:** *Bacillus thuringiensis* (*Bt*) is widely used to manage several lepidopteran insect pests including tobacco caterpillar, *Spodoptera litura* in groundnut. Nanoparticles (NPs) can make agricultural inputs like fertilizers and pesticides more effective and efficient and have shown the ability to enhance the insecticidal action of *Bt* when combined. They may increase the susceptibility of target insects to *Bt* toxins by damaging insect gut cells or interfering with their immune responses to develop nanostructured catalysts and to increase the Cfu/g with *Bt.* The current study is aimed to assess the impact NPs of on *Bacillus thuringiensis* (*Bt*) mass production under *in vitro* conditions.

**Methods:** The synthesis of Ca, Mg, Fe and Zn nanoparticles was carried out using sol-gel method. Characterization of the nanoparticles was done by using UV-vis spectrum, XRD, Particle size and zeta potential analysis, TEM and FT-IR techniques. These NPs were tested as catalysts in the production of biopesticide *Bt*.

**Result:** The synthesized and characterized NPs were clearly indicated that the prepared nanoscale oxide materials were highly stable and also been observed with uniform surface morphological features. The highest Colony forming units (Cfu)/gram (g) of *Bt* ($17.3\times10^9$. $16.9\times10^9$, $16.5\times10^9$ and $15.0\times10^9$) was recorded in treatments with 50 ppm MgO, 20 ppm CaO, 10 ppm ZnO and 50 ppm FeO (as against $6.7\times10^9$ Cfu/g in the control.

**Key words:** *Bacillus thuringiensis*, Characterization, Nanoparticles, Synthesis.

## INTRODUCTION

The insecticidal bacterium *Bt* has been proven to be one of the most effective tool for controlling lepidopteran insect pests including *S. litura* (Vimala devi *et al*., 2005). It is a naturally occurring, soil-dwelling bacterium that is widely used as a biological pesticide. It produces proteins that are toxic to certain insect pests. *Bt* toxins have been used as topical insecticides against lepidopteran pests and many others (Vimala devi and Vineela, 2014).

According to Dominguez (2004), calcium (Ca) ions support the maintenance of cell motility, transport, structure and differentiation processes such as sporulation, heterocyst formation and fruiting body growth. The divalent cation $Mg^{2+}$ is necessary for a number of enzymatic processes, including the regulation of membranes and ribosomes, neutralisation of nucleic acids and as a cofactor (Groisman *et al*., 2013). The most crucial cellular processes in which iron is involved are oxygen transport, Adenosine triphosphate (ATP) production, cell development and proliferation and detoxification (Duan *et al*., 2023). It is an enzyme coenzyme that catalyses the conversion of ribonucleotides to deoxyribonucleotidides, specifically the conversion of deoxyuridine to thymidine. Ribonucleotide reductase is a crucial enzyme for Deoxyribonucleic acid (DNA) production (Thelander *et al*., 1983). The survival of all living things depends on the metal ion Zn, which is engaged in numerous essential biological processes. They are present in every creature and are only found as parts of proteins, such as transcription factors, storage proteins and enzymes (Hood and Skaar, 2012).

The NPs exhibit distinctive chemical, physical and biological properties at a size of $10^{-9}$ m in diameter, as well as increased strength, strong electrical conductivity and additional chemical reactivity (Nykypanchuk *et al*., 2008, Sabbour, 2013, Nikita Sehgal *et al.,* 2023, Sharma Kumar Rajesh *et al*., 2022, Pabitra Barik, *et al*., 2023). Additionally, it is predicted that the creation of nanostructured catalysts

[1]Department of Entomology, Sri Venkateswara Agriculture College, Acharya N G Ranga Agricultural University, Lam, Guntur-522 034, Andhra Pradesh, India.
[2]KL College of Agriculture, KLEF, Green Fields, Vaddeswaram-522 502, Andhra Pradesh, India.
[3]Department of Soil Science, Institute of Frontier Technologies, Tirupati-517 502, Andhra Pradesh, India.

**Corresponding Author:** M. Gayathri, Department of Entomology, Sri Venkateswara Agriculture College, Acharya N G Ranga Agricultural University, Lam, Guntur-522 034, Andhra Pradesh, India. Email: gayathrimungara@gmail.com
ORCIDs: 0000-0002-6060-1516

**How to cite this article:** Gayathri, M., Venkateswarlu, N.C. and Prasad, T.N.V.K.V. (2025). Synthesis and Characterization of Ca, Mg, Fe and Zn Nanoparticles and its Impact on *Bacillus thuringiensis*. Agricultural Science Digest. 1-10. doi: 10.18805/ag.D-6142.

**Submitted:** 01-08-2024 **Accepted:** 09-12-2024 **Online:** 25-02-2025

in the upcoming years will enable pesticides to be more effective at lower doses. The present investigation aimed synthesis of metal nanoparticles and its impact of nanoparticles on multiplication and growth of *Bacillus thuringiensis*.

## MATERIALS AND METHODS

The present investigation on synthesis and characterization of Ca, Mg, Fe and Zn nanoparticles (NPs) was carried out at the Department of Entomology, Sri Venkateswara Agricultural College (SVAC) and Nanotechnology Laboratory, Department of Soil Science, Institute of Frontier Technology (IFT), Tirupati. Standardization of doses of nanomaterials with *Bt* (375 strain) was carried out in IFT, Regional Agricultural Research Station (RARS), Tirupati during *Kharif*, 2016-19.

### Synthesis and characterization of ZnNP, FeNP, CaNP and MgNP

The oxides of Zn, Fe, Ca and Mg were synthesized by using sol-gel method (Wahab *et al*., 2007) where oxide forms of nanoparticles were used. The homogeneous sol was produced from the precursors and converted into a gel. The solvent in the gel is then removed from the gel structure and the remaining gel is dried.

The properties of the dried gel depend significantly on the drying method and characterized using following methods.

### UV–Visible spectrum

Electronic transitions within the sample cause absorption in the near ultraviolet range. The apparent colour of the chemicals involved is directly impacted by the visible spectrum absorption. Understanding the electronic nature of the material's optical band gap aided by studying the spectral patterns of UV-Vis absorption.

### Fourier transform infrared spectroscopy (FTIR) analysis

The interferometer's intensity-time output is transformed into the intensity frequency of the groups of infra-red spectrum using a Fourier Transform. FTIR produces percentage transmission and wave number as its output, the atomic arrangement and concentrations of chemical bonds found in the materials have been identified.

### X-ray diffraction (XRD) analysis

XRD is used to find the structural determination of materials. The wave length of X-rays is on the atomic scale, so XRD is a primary tool for probing structure of materials.

### Particle size and zeta potential analysis

Nanopartical SZ-100 was used to quantify particle size and zeta potential (HORIBA). Dynamic light scattering is a method to record the hydrodynamic diameter (HDD) of the suspended particulates, while zeta potential helps in determining the bonding of the charged particles in dispersion.

### Transmission electron microscopy (TEM)

An electron beam is used in the TEM technique to image the sample's surface, giving it a much higher resolution than is feasible with light-based imaging methods. To directly measure the size, shape, size distribution and morphology of NPs, TEM is the technique of choice. We used a JEOL 1010 transmission electron microscope with a 100 keV accelerating voltage and an AMT XR41-B 4-megapixel (2048) bottom mount CCD camera for the current study. For magnifications up to 150,000x, the camera's finite-conjugate optical coupler offers excellent resolution, flat focus and less than 0.1% distortion (Surender and Sunithdevi (2010) and Robina *et al.* (2013).

### Effect of NPs on multiplication and growth of *Bt*

### Preparation of nanosolutions

In order to investigate the catalytic activity of nanomaterials on the *Bt*, Zn, Fe, Ca and Mg at 10 ppm, 20 ppm, 50 ppm, 100 ppm and 500 ppm were added to the Luria Bertani Agar media in a 1:9 ratio (1ml of nanoparticulate solution to 9 ml of Luria Bertani Agar (LBA) media). This was done before sterilization.

### Inoculation of *Bt*

A single loop of bacteria (*Bt* strain 375) was placed into 1 ml of Luria Bertani (LB) broth and kept as such for 24 hours at 25°C. Then, the culture was diluted $10^{-9}$ times in sterile water by serial dilution method. A total of 0.1 ml from the sample was inoculated into LBA media impregnated with metal nanoparticles and spread with an L-shaped rod and covered in glass lid nder a laminar air flow chamber. These dishes of 21 treatments with 3 replications were incubated for 24 hours at 28°C (Plate 1).

### Colony assessment

The colony forming units (Cfu) of *Bt* were counted with the aid of a colony metre after 24-hours of incubation as per the formular proposed by formula (Vimala devi and Vineela 2014).

$$\text{Cfu/g} = \frac{\text{Average number of colonies} \times \text{Dilution factor}}{\text{Volume plated}}$$

### Statistical analysis

Completely Randomized Design (CRD) statistical method used to standardize the effective concentration of different NPs on *Bt* cfu/g in present studies.

## RESULTS AND DISCUSSION

### Characterization of CaO, MgO, FeO and ZnO nanoparticles

### UV-Vis Spectroscopy

UV-Vis spectroscopy recorded the absorbance peak of CaONPs at 340 nm, while MgONPs at 310 nm, FeONPs at 370 nm and ZnONPs at 300 nm suggesting successful formation of nanoparticles (Fig 1 to 4).

**Fourier transform infrared (FTIR) spectroscopy**

**CaO**

The spectrum showed the bands for the functional groups located at 3419, 2191, 1420, 680, 825 $cm^{-1}$. The peaks at 3419 and 2191represent the presence of -OH group and medial alkyne di substitution respectively. Skeletal C-C vibrations were recorded consecutively from 985 $cm^{-1}$ to 877 $cm^{-1}$. The bands near 680 $cm^{-1}$ and 693$cm^{-1}$ indicates the presence of aryl thioesters. (Fig 5).

**MgO**

The spectrum showed the bands for the functional groups located at 2064, 713 and 1388 $cm^{-1}$. The peaks at 2064 and 1388 $cm^{-1}$represent the presence of isothiocyanate group and trimethyl/3º butyl groups respectively. Skeletal C-C vibrations were recorded at 713 $cm^{-1}$. (Fig 6).

**FeO**

The spectrum displays the peaks for the functional groups located at 2119, 1908, 1459, 1654 and 1131 $cm^{-1}$ while the peak at 2119 represents the cyanide / thiocyanate or related ions and 1908 denotes aromatic combination bands. Aromatic ring stretch was recorded at 1459 $cm^{-1}$, open chain imino groups and C-C vibrations were evident from the bands near 1654 $cm^{-1}$ and 1131 $cm^{-1}$ respectively (Fig 7).

**ZnO**

The peaks in the spectrum refer to the functional groups located at 1460, 1886, 1457 and 1371 $cm^{-1}$. The peaks at 1460 and 1371 represent the presence of methyl C-H asymmetric / symmetric band whereas the peak at 1886 $cm^{-1}$ refers to the presence of transition metal carbonyls. Carbonate ion was recorded at 1457 $cm^{-1}$ band and to conclude, the change in wave number of the functional groups might due to the synthetic protocol (Fig 8).

**X-ray diffraction (XRD) analysis**

The CaO's XRD pattern demonstrates that the cubic CaO can be used to identify the NPs. Their lattice parameters match the standard numbers provided in JCPDS PDF 82-1690 quite well (CaO). The diffraction intensities were recorded from 10°-80° at 2θ. Seven different and important characteristic peaks recorded at 32.2°, 35.7°, 37.3°, 48.5°, 54.5°, 64.5° and 67.3° correspond to the (111), (110), (200), (024), (202), (311) and (222) crystal planes, respectively (Fig 4.3.1). Using Scherrer's equation, the average crystallite size (3.15 nm) was calculated from the broadenings of matching peaks:

$$D = 0.94\lambda/\beta\cos\theta$$

Where,

D= Average crystallite domain size perpendicular to the reflecting planes.

$\lambda$ ($1.5429 \times 10^{-10}$)= X-ray wave length of the incident beam in nm.

$\theta$= Diffraction angle.

$\beta$= Full width at half the maximum intensity in radians (Fig 9).

The hexagonal phase of MgO in the synthesised substance was demonstrated by the XRD pattern. The absence of impurities in this pattern suggests that hexagonal phase MgO could be produced using the current synthetic method and all of the crystal structures complied with the JCPDS data that had been published. The Scherrer

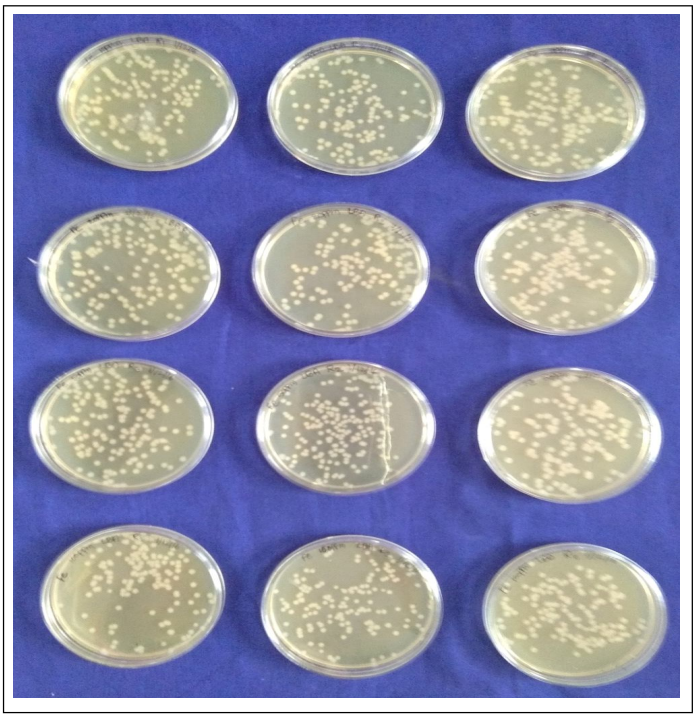

**Plate 1:** *Bt* colony forming units at $10^9$ serial dilution grown under different nano based LBA media.

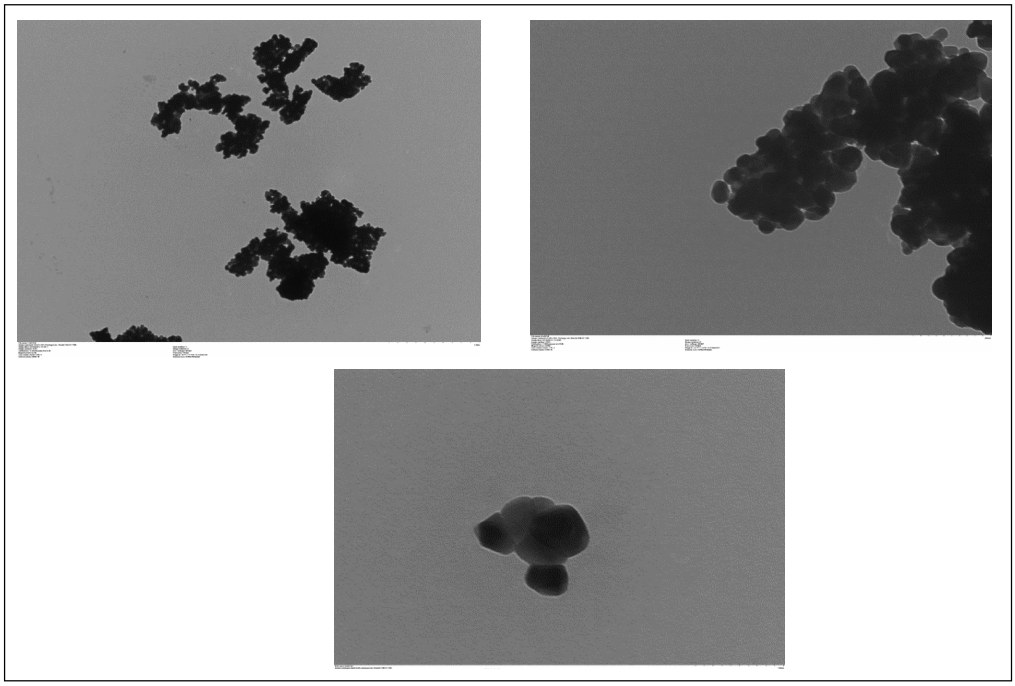

**Plate 2:** TEM image of synthesized nanocalcium particles.

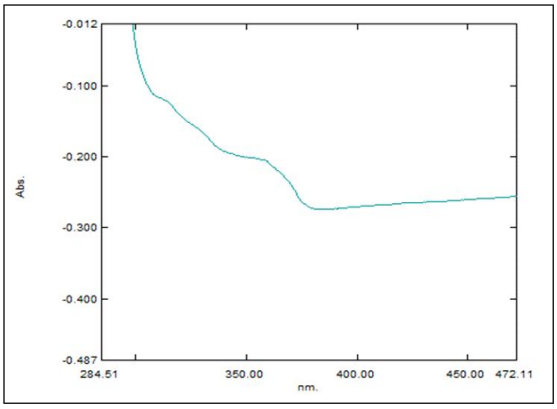


**Fig 1:** UV-visible absorption spectrum for synthesized calcium oxide nanoparticles.

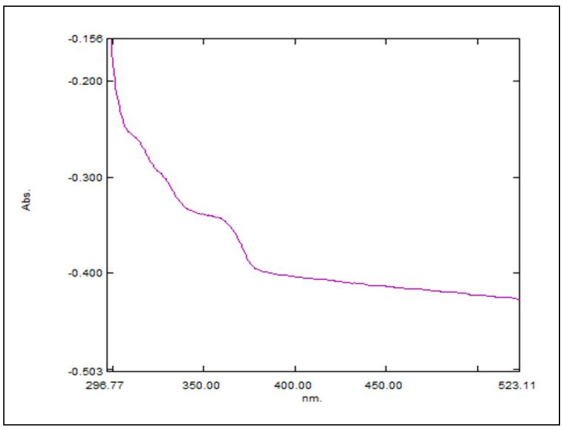


**Fig 3:** UV-visible absorption spectrum for synthesized ferrous oxide nanoparticles.

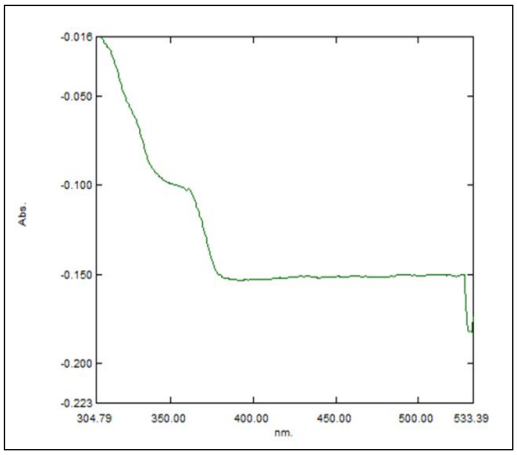


**Fig 2:** UV-visible absorption spectrum for synthesized magnesium oxide nanoparticles.

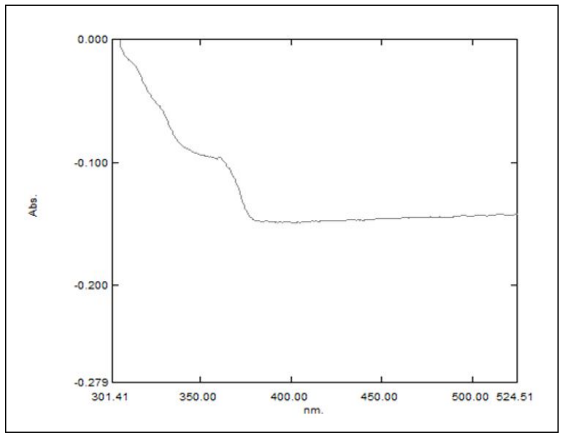


**Fig 4:** UV-visible absorption spectrum for synthesized zinc oxide nanoparticles.

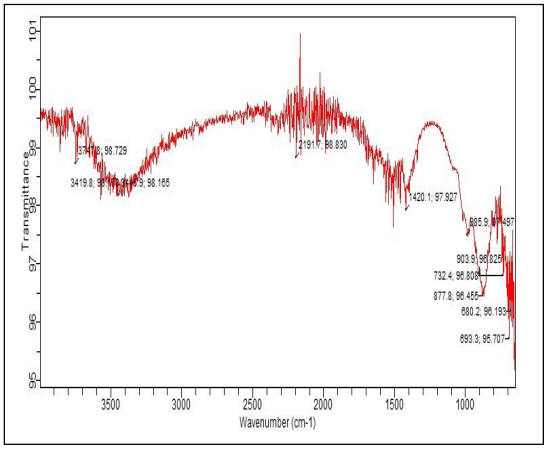


**Fig 5:** CaONPs.

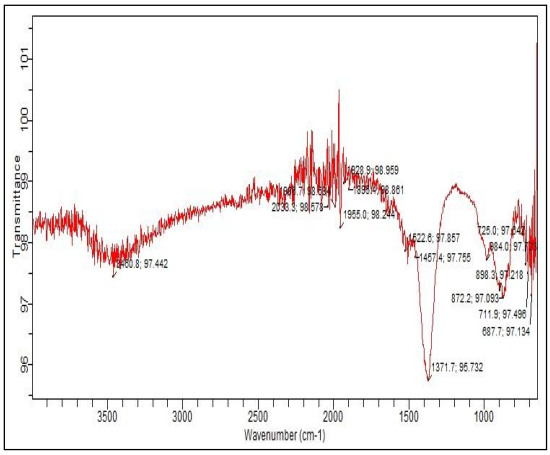


**Fig 8:** ZnONPs FT-IR micrograph confirming the presence of different functional groups on the surface of the nanoparticles.

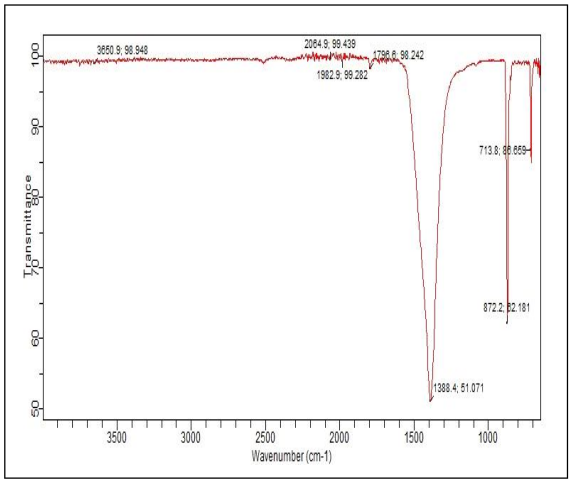


**Fig 6:** MgONPs.

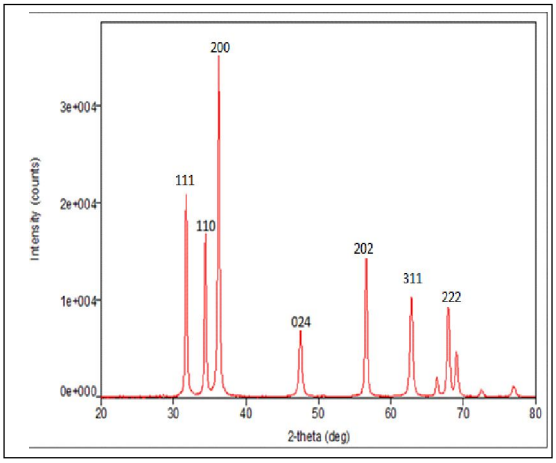


**Fig 9:** XRD image for synthesized nanocalcium oxide.

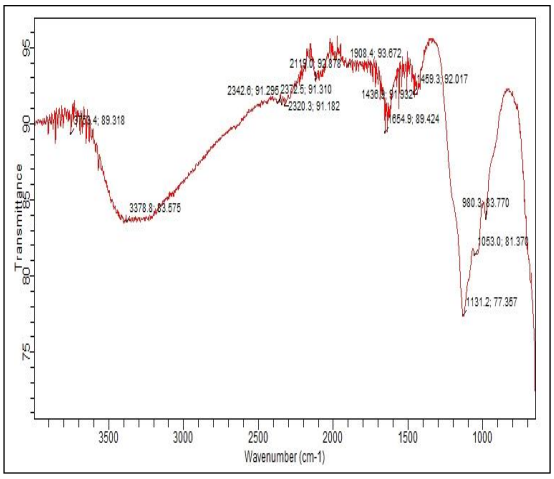


**Fig 7:** FeONPs FT-IR micrograph confirming the presence of different functional groups on the surface of the nanoparticles.

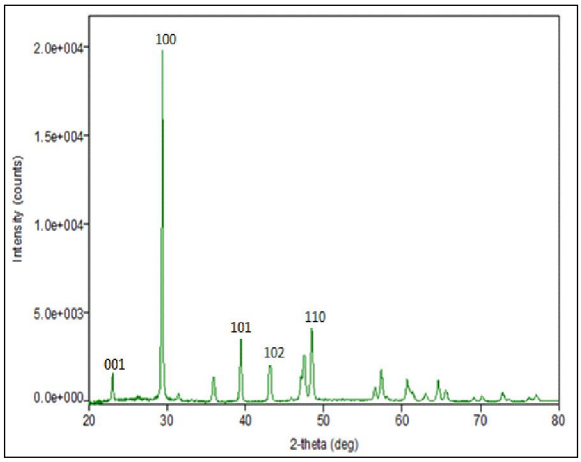


**Fig 10:** XRD image for synthesized nanomagnesium oxide.

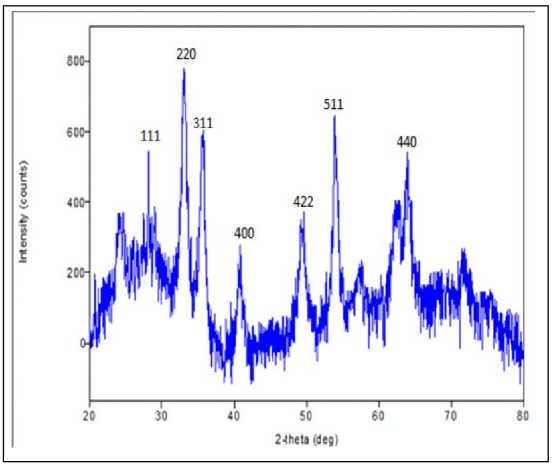


**Fig 11:** XRD image for synthesized nanoferrous oxide.

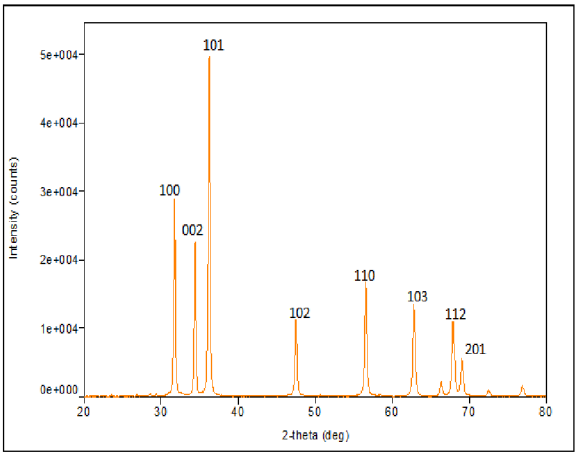


**Fig 12:** XRD image for synthesized nanozinc oxide.

formula was used to determine the size of the crystallites and was applied to the main peaks (Fig 10)

The examples are polycrystalline and primarily contain (100), (101) and (110) MgO, according to the XRD pattern. Within the XRD measurement range, no additional peaks could be located. It is discovered that the respective peak intensities for (100), (101) and (110) are greater than 2. (4.3.3). It has been demonstrated that polycrystalline MgO barriers with a higher percentage of the (100) textured phase produce very high values (Fig 11).

The crystalline of the samples was analyzed by powder XRD. The diffraction profiles of FeO NPs samples shown some disturbance peak there is only one major peak seen ( theta angle at 35.5°) showing (220) indicating the presence of FeO, 28.7° showing (111), 38.9° showing (311), 41.2° showing (400), 48.9° showing (422), 55.4° showing (511) and 66.4° showing (220)

All peaks were found to correspond to an FeO spinel structure and this observation is significant as it mainly consist of magnetite partially oxidized at their surface (Fig 11).

The prepared material contains particles in the nanoscale region, as indicated by a clear line broadening of the XRD peaks. Our study of the XRD patterns allowed us to identify the peak's intensity, position and width as well as its full-width at half-maximum (FWHM) data. The hexagonal wurtzite phase of ZnO has been sharply enumerated as the diffraction peaks at 31.84°, 34.52°, 36.33°, 47.63°, 56.71°, 62.96°, 68.13° and 69.18° (Fig 12). The fact that the XRD lines have widened indicates that the material contains NPs. Some notable peaks in the XRD were taken into consideration and the associated d-values were compared to the norm [JCPDS file No. 80-0075]. The

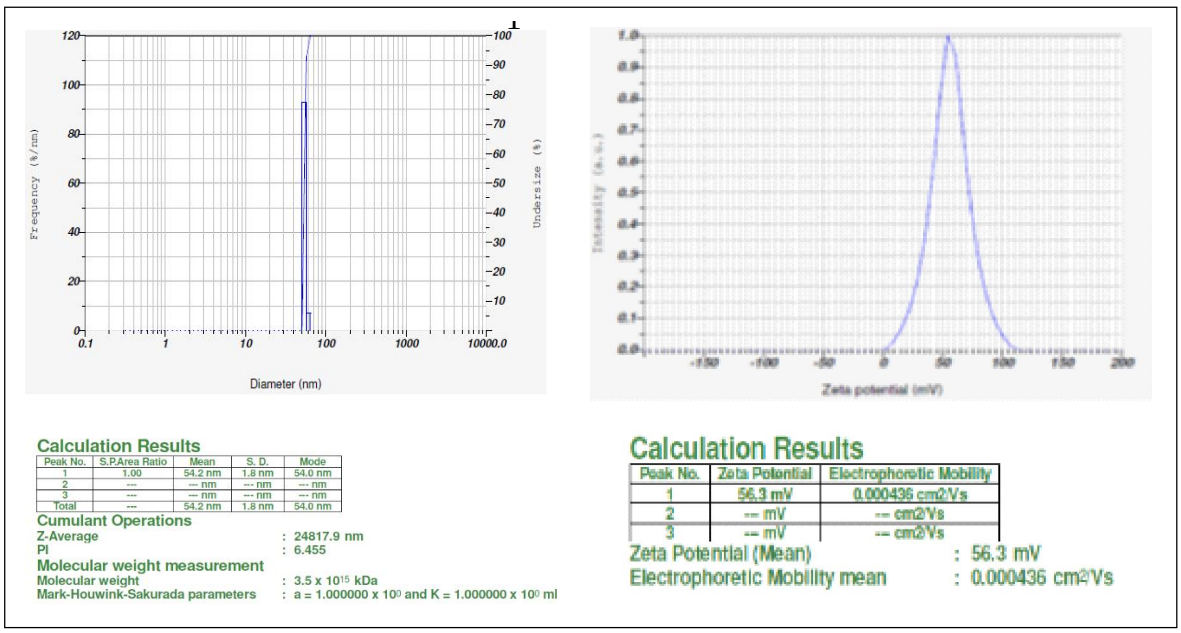


**Fig 13:** Histogram of nanoferrous particle size and zeta potential.

hexagonal structure of pure ZnO in the metal oxide was verified by X-ray diffraction.

**Particle size and zeta potential analysis**

The measured hydrodynamic diameter (HDD) of ZnO NPs was 42.7 nm and that of CaO, MgO NPs and FeO NPs were 98.5 nm, 36.8 nm and 112.2 nm respectively Greater stability of the prepared NPs is indicated by a larger zeta potential value. The measured HDD of the prepared nanoscale oxide particles (Zn, Ca, Mg and Fe) were well comparable with the measured sizes (25 nm, 50 nm, 30 nm and 80 nm) from the TEM micrographs.

Zeta potential of the substance is an important indicator of the stability of the respective substance. The measured zeta potentials of nanoscale ZnO, CaO, MgO and FeO were -20.1 mV, -28.9 mV, -44.7 and -20.1mV, respectively clearly indicated that the prepared nanoscale oxide materials were highly stable (Fig 13 to 16).

**TEM analysis**

The micrographs of transmission electron microscope showed well defined, monodispersed nanoscale oxide particles of Ca, Fe, Mg and Zn. From the micrographs relatively spherical shaped CaO NPs were observed with the mean particle size of 60nm. Slight agglomeration of the particles was observed and is due to the absence of protective ligands on the surface of the NPs (Plate 2 to 5) Rod shaped and occasional spherical shaped FeO NPs monodispersity with the slight agglomeration of FeO NPs also been observed with uniform surface morphological features and with mean size of 80 nm.

Relatively spherical shaped MgO NPs with mean size of 50nm. The agglomeration of the particles is due to the absence of the protective ligands on the surface.

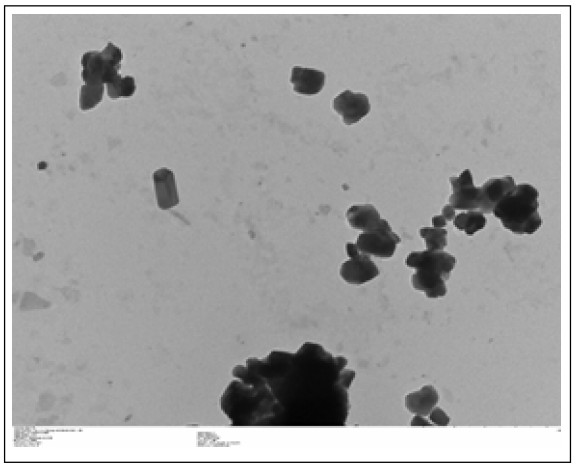

**Plate 3:** TEM image of synthesized nanomagnesium particles.

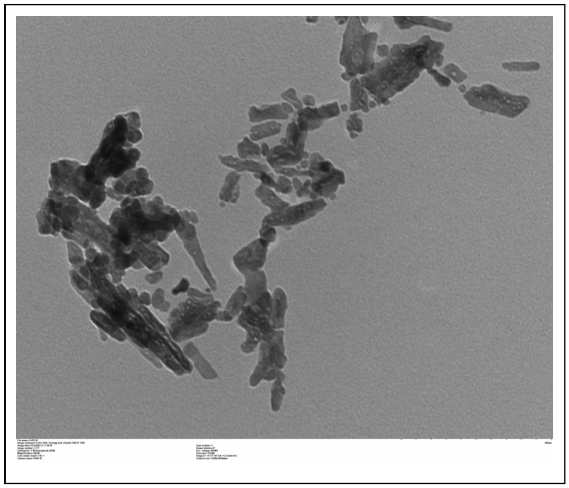

**Plate 4:** TEM image of synthesized nanoferrous particles.

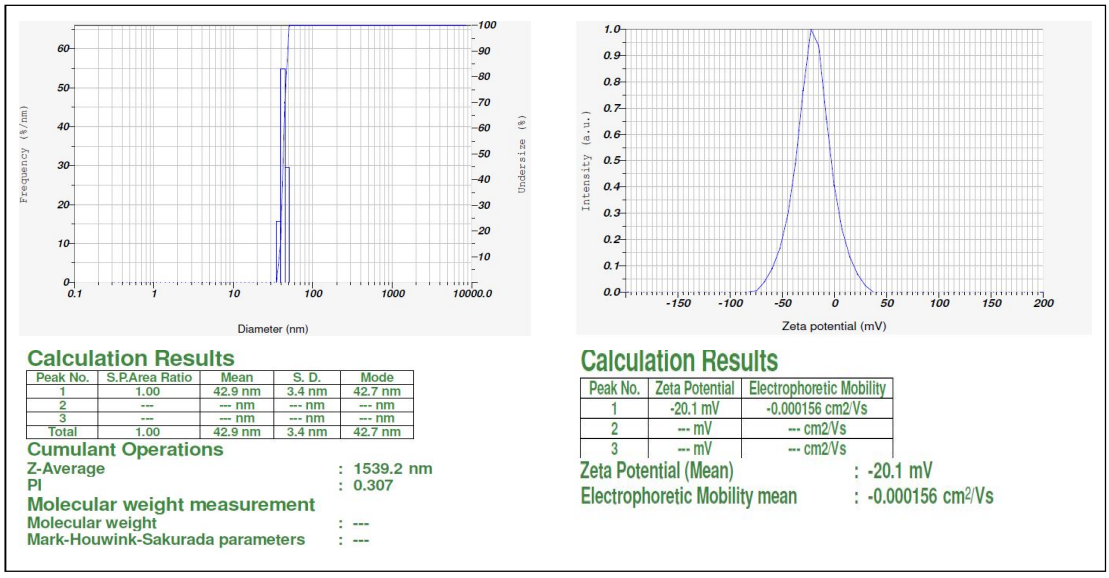


**Fig 14:** Histogram of nanozinc particle size and zeta potential.

Polydispersed spherical shaped ZnO NPs with mean size of 25nm. The absence of the protective ligands on the surface caused the agglomeration of the NPs (Table 1).

The results pertaining to characterisation of nanoCaO using UV-absorbance spectrum, FTIR and XRD, DLS and TEM were closely related with Ashwini *et al*. (2016) and Mirghiasi *et al*. (2014). The synthesis and characterisation of nanoMgO was closely related to Wahab *et al*. (2007), Suresh *et al*. (2014) and Agarwal *et al*. (2015). The nanoFeO synthesis and characterisation results were in close conformity with Surender and Sunithadevi (2010). Similarly the nanoZnO characterisation results were in agreement with Vafaeea and Sasani (2007), Robina *et al*. (2013) and Jurablu *et al*. (2015).

**Effect oof nanoparticles on *Bt***

The maximum cfu count ($17.3\times10^9$ Cfu/g) was recorded with MgO at 50 ppm concentration followed by $9.8\times10^9$ with 100 ppm, $8.4\times10^9$ with 500 ppm and 20 ppm and $7.8\times10^9$ with 10 ppm. Similarly, $16.9\times10^9$ with CaO 20 ppm, $14.3\times10^9$ with 50 ppm, $8.4\times10^9$ with 100 ppm, $8.1\times10^9$ with 10 ppm and $7.4\times10^9$ with 500 ppm. Simultaneously with ZnO the maximum number of $16.5\times10^9$ Cfu/g recorded at 10 ppm, followed by $10.7\times10^9$, $8.4\times10^9$, $7.8\times10^9$ and $7.4\times10^9$ with 20 ppm, 50 ppm, 100 ppm and 500 ppm respectively. With FeO the highest number of $15.0\times10^9$ Cfu/g recorded with 50 ppm, followed by $9.1\times10^9$ with 100 ppm, $8.9\times10^9$ with 10 ppm, with 500 ppm, $8.3\times10^9$ with 20 ppm, as against $6.7\times10^9$ Cfu/g in control (Table 2). During 2017, the maximum number of $17.3\times10^9$ Cfu/g were recorded with MgO at 50 ppm concentration followed by $16.9\times10^9$ with CaO at 20 ppm, $16.5\times10^9$ with ZnO at 10 ppm, $15.0\times10^9$ Cfu/g with FeO at 50 ppm as against $6.7\times10^9$ Cfu/g in control.

UV absorption spectrums of the CaO nano-particles band positions at 300 and 365 nm correspond to CaO NPs. The UV spectrum of Ca NPs shows the absorbent peak rose at 340 nm. The formation of MgO NPs metal oxide in the material is indicated by the absorbance at 310 nm from UV-visible spectroscopy.

Prepared and annealed $Fe_2O_3$ NPs were achieved at wavelength near 370 nm whereas for ZnO NPs the peak o*Bt*ained at 300 nm clearly demonstrates the presence of the reaction mixture.

The nanoCa spectrum showed the bands for the functional groups located at 3419, 2191, 1420, 680, 825 $cm^{-1}$. The peaks at 3419 and 2191 represent the presence of –OH group and medial alkyne disubstitution respectively. Skeletal C-C vibrations were recorded consecutively from 985 $cm^{-1}$ to 877 $cm^{-1}$. The bands near 680 $cm^{-1}$ and 693 $cm^{-1}$ indicates the presence of aryl thioesters.

The nanoMgO spectrum showed the bands for the functional groups located at 2064, 713, 1388 $cm^{-1}$. The peaks at 2064 and 1388 $cm^{-1}$ represent the presence of isothiocyanate group and trimethyl/3º butyl groups respectively. Skeletal C-C vibrations were recorded at 713 $cm^{-1}$.

The nanoFeO spectrum displays the peaks for the functional groups located at 2119, 1908, 1459, 1654, 1131 $cm^{-1}$. 2119 represents the cyanide/thiocyanate or related ions at 1908 $cm^{-1}$ denotes aromatic combination bands. Aromatic ring stretch was recorded at 1459 $cm^{-1}$, open chain imino groups and C-C vibrations were evident from the bands near 1654 $cm^{-1}$ and 1131 $cm^{-1}$ respectively.

The nanoZnO peaks in the spectrum refer to the functional groups located at 1460, 1886, 1457, 1371 cm-1. The peaks at 1460 and 1371 represent the presence of methyl C-H asymmetric/symmetric bend whereas the peak at 1886 $cm^{-1}$ refers to the presence of transition metal carbonyls.

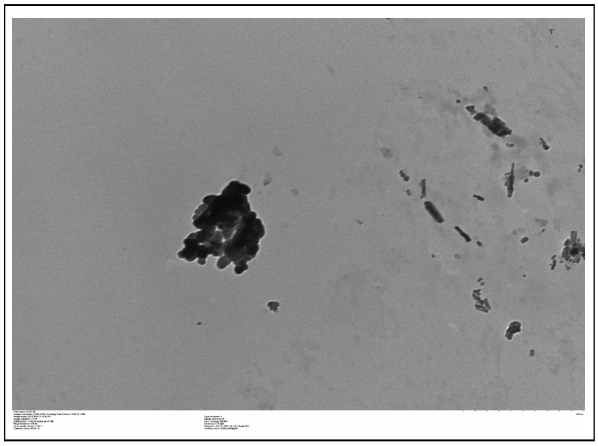

**Plate 5:** TEM image of synthesized nanozinc particles.

**Table 1:** Characterization of synthesized NPs.

| Nano-particles | UV | FTIR | XRD | PSA | TEM |
|---|---|---|---|---|---|
| Ca | 340 nm | Functional groups located at 3419, 2191, 1420, 680, 825 $cm^{-1}$. | 111, 110, 200, 202, 311 and 222 crystal planes indicates cubic structure | 40 nm, -28.5 mV | 50 nm |
| Mg | 310 nm | 2064, 713, 1388 $cm^{-1}$. | 100, 101 and 110 MgO hexagonal structure | 37.4 nm, -44.7 mV | 30 nm |
| Fe | 370 nm | 2119, 1908, 1459, 1654, 1131 $cm^{-1}$ | 111, 220, 311, 400, 422, 511, 440 spinel shape | 54.2 nm, 56.3 mV | 80 nm |
| Zn | 300 nm | 1460, 1886, 1457, 1371 $cm^{-1}$. | 100, 101, 102, 110 hexagonal shape | 42.9 nm, -201. mV | 25 nm |

**Table 2:** Influence of different NPs on *B. thuringiensis* (Cfu $g^{-1}$) in LBA media at different concentrations.

| Name of the treatment | Concentration | No.of Cfu/g 2017 |
|---|---|---|
| MgO (MgO) | 10 ppm | $7.8 \times 10^{9cde}$ |
| MgO (MgO) | 20 ppm | $8.4 \times 10^{9cde}$ |
| MgO (MgO) | 50 ppm | $17.3 \times 10^{9a}$ |
| MgO (MgO) | 100 ppm | $9.8 \times 10^{9cde}$ |
| MgO (MgO) | 500 ppm | $8.4 \times 10^{9e}$ |
| CaO (CaO) | 10 ppm | $8.1 \times 10^{9cde}$ |
| CaO (CaO) | 20 ppm | $16.9 \times 10^{9a}$ |
| CaO (CaO) | 50 ppm | $14.3 \times 10^{9ab}$ |
| CaO (CaO) | 100 ppm | $8.4 \times 10^{9cde}$ |
| CaO (CaO) | 500 ppm | $7.4 \times 10^{9e}$ |
| ZnO (ZnO) | 10 ppm | $16.5 \times 10^{9a}$ |
| ZnO (ZnO) | 20 ppm | $10.7 \times 10^{9c}$ |
| ZnO (ZnO) | 50 ppm | $8.4 \times 10^{9cde}$ |
| ZnO (ZnO) | 100 ppm | $7.8 \times 10^{9cde}$ |
| ZnO (ZnO) | 500 ppm | $7.4 \times 10^{9de}$ |
| FeO ($Fe_2O_3$) | 10 ppm | $8.3 \times 10^{9cde}$ |
| FeO ($Fe_2O_3$) | 20 ppm | $9.1 \times 10^{9bc}$ |
| FeO ($Fe_2O_3$) | 50 ppm | $15.0 \times 10^{9ab}$ |
| FeO($Fe_2O_3$) | 100 ppm | $8.9 \times 10^{9cde}$ |
| FeO ($Fe_2O_3$) | 500 ppm | $7.7 \times 10^{9cde}$ |
| Control | | $6.7 \times 10^{9de}$ |
| C.D. | | 8.90 |
| SE(m) | | 3.10 |
| SE(d) | | 4.3 |
| C.V. | | 2.59 |

The CaO's XRD pattern demonstrates that the cubic CaO can be used to identify the NPs. Their lattice parameters match the standard numbers listed in JCPDS PDF# 82-1690 quite well (CaO).The diffraction intensities were recorded from 10°-80° at 2è. Seven different and important characteristic peaks recorded at 32.2°, 35.7°, 37.3°, 48.5°, 54.5°, 64.5° and 67.3° correspond to the (111), (110), (200), (024), (202), (311) and (222) crystal planes, respectively.

XRD pattern proved that the synthesized material is MgO of hexagonal phase. The crystalline of the samples was analyzed by powder XRD. The diffraction profiles of FeO NPs samples showed some disturbance peak with only one major peak observed (220) ( theta angle at 35.5°) indicating the presence of FeO 111 at 28.7°, 311 at 38.9°, 400 at 41.2°, 422 at 48.9°, 511 at 55.4° and 220 at 66.4°.

All peaks were found to correspond to an FeO spinel structure and this observation is significant as it mainly consisted of magnetite partially oxidized at their surface.

ZnO NPs' XRD results revealed a distinct line broadening of the XRD peaks, indicating that the prepared substance contained nanoscale-sized particles. The peak intensity, position and width from this study of the XRD patterns using full width at half-maximum (FWHM) data. It has been determined with great precision that the diffraction maxima at 31.84°, 34.52°, 36.33°, 47.63°, 56.71°, 62.96°, 68.13° and 69.18° belong to the hexagonal wurtzite phase of ZnO.

The measured hydrodynamic diameter (HDD) of ZnO NPs was 42.7 nm and that of CaO, MgO NPs and FeO NPs were 98.5 nm, 36.8 nm and 112.2 nm, respectively. The measured hydrodynamic diameters of the prepared nanoscale oxide particles (Zn, Ca, Mg and Fe) were well comparable with the measured sizes (25 nm, 50 nm, 30 nm and 80 nm) from the TEM micrographs.

Zeta potential of the substance is an important indicator of the stability of the respective substance. The measured zeta potentials of nanoscale ZnO, CaO, MgO and FeO were -20.1 mV, -28.9 mV, -44.7 and -20.1 mV respectively which clearly indicated that the prepared nanoscale oxide materials were highly stable.

The micrographs of transmission electron microscope showed well defined, monodispersed nanoscale oxide particles of Ca, Fe, Mg and Zn.

The NPs enriched media recorded maximum cfu/g was with *B.thuringiensis* with MgO at 50ppm, CaO at 20 ppm, ZnO at 10 ppm and FeO 50 ppm. The results are on par with Dominguez, 2004, Groisman *et al.*, 2013, Duan *et al.*, 2023, Hood and Skaar, 2012 who identified the Calcium (Ca), $Mg^{2+}$, Zn and iron ions importance in sporulation, enzymatic processes including the regulation of

membranes and ribosomes, cell development and proliferation and for the synthesis of proteins and enzymes respectively.

## CONCLUSION

The synthesis of NPs *viz*., Mg, Ca, Fe and Zn were carried out by using sol-gel method. Characterisation of synthesized NPs was done by using UV-visible spectrum, Zeta potential analyser, FTIR, XRD and TEM.

Characterization of NPs revealed that the particles were of 25 to 80 nm size, zeta potential of 25 to 60 mV with spherical (Cao) and rod shaped (FeO) structures, with good electronic transitions that demonstrated the presence of the reaction mixture, presence of atomic arrangement and the concentrations of the chemical bonds. Maximum cfu/g was recorded with *B.thuringiensis* with MgO at 50ppm, CaO at 20 ppm, ZnO at 10 ppm and FeO 50 ppm.

## ACKNOWLEDGEMENT

I extend my immense thanks to S.V.AGRICULTURE COLLEGE AND IFT TIRUPATHI, ANGRAU for providing financial assistance and all other facilities for my research work.

### Disclaimers

The views and conclusions expressed in this article are solely those of the authors and do not necessarily represent the views of their affiliated institutions. The authors are responsible for the accuracy and completeness of the information provided, but do not accept any liability for any direct or indirect losses resulting from the use of this content.

### Conflict of interest

There are no conflicts of interest regarding the publication of this article.

## REFERENCES

Agarwal, R.M., Charpe, S.D., Raghuwanshi, F.C., Lamdhade, G.T. (2015). Synthesis and Characterization of MgO NPs with 1:1 molar ratio *via* Liquid-Phase Method. International Journal of Application or Innovation Engineering Management. 4(2): 141-145.

Ashwini, A., Ramalakshmi, S., Mary, G. (2016). Green Synthesis of CaO NPs and Its Applications. International. Journal of. Engineering. Research. Application. 6(10): 27-31.

Dominguez, C.D. (2004): Ca signalling in bacteria. Molecular Microbiology. 54(2): 291-297.

Groisman, E.A, Hollands, K., Kriner, M.A., Lee1, E.J., Park, S.Y., Mauricio, H. (2013). Pontes. Bacterial Mg2+ homeostasis, transport and virulence. Annual Review of Genetics. 47: 625-646.

Duan, G., Li, J., Duan, Y., Zheng, C., Guo, Q., Li, F., Zheng, J., Yu, J., Zhang, P., Wan, M (2023): Mitochondrial iron metabolism: The crucial actors in diseases. Molecules. https:// doi.org/ 10.3390/molecules28010029.

Hood, M.I., Skaar, E.P. (2012): Nutritional immunity: Transition metals at the pathogen-host interface. Nature Reviews Microbiology. 10: 525-537.

Jurablu, S., Farahmandjou, M., Firoozabadi, T.P. (2015). Sol-Gel Synthesis of ZnO (ZnO) NPs: Study of Structural and Optical Properties. Journal of . Sciences. Islamic. Republic of Iran. 26 (3): 281-285.

Mirghiasi, Z., Bakhtiari, F., Darezereshki, E., Esmaeilzadeh, E. (2014). Preparation and characterization of CaO NPs from $Ca(OH)_2$ by direct thermal decomposition method. Journal of Industrial and Engineering Chemmistry m. 20(1): 113-117.

Sehgal, N., Naresh, G., Kumari, A. (2023) Latest Developments and Applications of Nanotechnology in Agriculture Sector: A review. Agricultural reviews. 44(3): 275-288. doi: 10.18805/ag.R-2175.

Nykypanchuk, D., Maye, M., Lelie, V.D., Gang, O. (2008). DNA-guided crystallization of colloidal nano particles. Nature. 451(7178): 549-552.

Barik, P., Saharan, N., Krishnani, K.K., Vardia, H.K., Sharma,R., Malik, M.A. (2023). Bacteria-mediated synthesis of iron oxide nanoparticles and their efficiency in ammonia removal from fish culture tanks. Indian Journal of Animal Research. 57(10): 1397-1406. doi: 10.18805/IJAR.B-5090.

Robina, A., Saira. R., Rehman, M.K., Naseem, S. (2013). Synthesis and Characterization of ZnO NPs. The world congress on Advances in nano, Biomechanics, Robotics and Energy Research. pp 287-296.

Sabbour, M.M. (2013). Entomotoxicity assay of Nano-particle 3-(ZnO ZnO) Against *Sitophilus oryzae* under laboratory and store conditions in Egypt. Scientific. Reearchs. Reports. 1(2): 51-57.

Rajesh, S.K., Shubham, M.K., Kavita A., Bhuri, S., Hemraj, C., Maurya, I.B. (2022). Influence of Zn, Fe and Ag nanoparticles on growth, yield attributes and profitability in tomato (*Solanum lycopersicum* mill). Agricultural Reviews. 43(4): 511-515. doi: 10.18805/ag.R-2448.

Surender, D., Sunitadevi, S. (2010). Synthesis and structural characterization of iron oxide-silica nanocomposites prepared by the solgel method. International Journal of Electronic Engineering. 2(1): 89-92.

Suresh, J., Yuvakkumar, R., Sundrarajan, M., Hong, S.I. (2014). Green synthesis of MgO NPs. Advanced Materials. Research. 952: 141-144.

Thelander, L., Graslund, A., Thelander, M. (1983) Continual presence of oxygen and iron required for mammalian ribonucleotide reduction: Possible regulation mechanism. Biochemistry. Biophysics. Research. Communication. 110: 859-865.

Vafaeea, M and Sasani, G.M. (2007). Preparation and characterization of ZnO NPs by a novel sol–gel route. Material letters. 61(14-15): 3265-3268.

Vimala Devi, P.S., Ravinder, T. and Jaidev, C. (2005). Barley based medium for the cost effective production of *Bacillus thuringiensis*. World Journal of Microbiology and Biotechnology. 21: 173-178.

Vimala Devi, P.S., Vineela, V. (2014). Suspension concentrate formulation of *Bacillus thuringiensis* var. kurstaki for effective management of *Helicoverpa armigera* on sunflower (*Helianthus annuus*). Biocontrol Science and Technology. 25(3): 329-336.

Wahab, R., Ansari, S.G., Dar, M.A., Kim, Y.S., Shin, H.S. (2007). Synthesis of MgO NPs by sol-gel process. Material Science Forum. 558-559: 983-986.